Summer 7-2-2018

Development of MOF@Polymer Composite Materials Through Bottom-Up Self-Assembly Techniques

Roberto C. Arbulu

Roberto Christian Arbulu

Candidate

Chemistry and Chemical Biology

Department

This thesis is approved, and it is acceptable in quality and form for publication:

Approved by the Thesis Committee:

Dr. Yang Qin , Chairperson

Dr. Martin Kirk

Dr. Jeffrey Rack

DEVELOPMENT OF MOF@POLYMER COMPOSITE MATERIALS THROUGH BOTTOM-UP SELF-ASSEMBLY TECHNIQUES

by

ROBERTO CHRISTIAN ARBULU

B.S., CHEMISTRY AND BIOCHEMISTRY,
FLORIDA STATE UNIVERSITY, 2014

THESIS

Submitted in Partial Fulfillment of the
Requirements for the Degree of

Master of Science

Chemistry

The University of New Mexico
Albuquerque, New Mexico

July, 2018

DEDICATION

To my father and mother for their endowments, encouragement, and guidance and to my wife for her continued love and support.

ACKNOWLEDGEMENTS

First and foremost, I would like to give a special thank you my advisor Dr. Yang Qin, who has helped guide me through this process. His expertise and leadership have helped me to grow in the lab and in life. Additionally, I would like to extend my gratitude to my committee, Dr. Jeffrey Rack and Dr. Martin Kirk, whose constructive criticism and engaging conversations have encouraged me to always be at my best. I would also like to thank my lab mates for their help and support over the last few years. Finally, I would like to acknowledge the faculty and staff of the University of New Mexico Department of Chemistry and Chemical Biology, whose support was critical for my success.

Development of MOF@Polymer Composite Materials Through Bottom-Up Self-Assembly Techniques

by

Roberto Christian Arbulu

B.S., Chemistry and Biochemistry, Florida State University, 2014
M.S., Chemistry, University of New Mexico, 2018

ABSTRACT

MOF-based mixed matrix membranes (MMMs) are a promising new class of MOF/polymer composite materials. Currently, fabrication of MMMs is based on top-down methods with limited control over MOF positioning, integration, or morphology. This work focuses on the growth of well-defined one-dimensional (1-D) MOF nanostructures within the pores of a nanoporous polymer template, either commercially available or through the self-assembly of block co-polymers having tailor-designed surface functionalities. Studies were conducted using zeolitic imidazole framework-8 (ZIF-8) and polycarbonate track etched (PCTE) membranes, which demonstrated the feasibility of the outlined approach, and revealed the formation of distinct super- and nanostructures with controlled morphologies and orientations through variations in reactant concentrations and pore dimensions. A combination of electron microscopy and X-Ray techniques were used to fully characterize the new templated MMMs and identify the key factors that contribute to crystal growth and help determine the underlying mechanism for growth. Additionally,

new polymeric materials were targeted and synthesized which will ultimately lead to the fabrication of designer block co-polymer asymmetric membranes for the in-situ growth of MOF.

TABLE OF CONTENTS

LIST OF FIGURES

LIST OF TABLES

Chapter 1.

Introduction

Industrial separation technology is an exploding field due to the high demand of pure chemical products. The current collection of separation techniques available to industry include Distillation, Evaporation, Drying, Extraction, Absorption, Adsorption, Membrane, Crystallization and Physical methods. This combination of processes accounts for ten to fifteen percent of the worlds energy consumption with thermal methods, such as distillation, accounting for more than eighty percent of this total.[1] Membrane based separations, which presently account for less than three percent of the total energy costs, have the potential to dramatically decrease the annual costs attributed to industrial separations by about four billion dollars and considerably reduce our impact on the environment.[2] More specifically, membrane-based gas are pressure driven processes that consume less energy, use less space, have no moving parts, and operate in a continuous mode making them easily applicable to remote locations such as offshore oil platforms.[3] Two factors dictate the economics of gas separation membranes, selectivity and permeability, and both factors are controlled by the membrane materials structure and composition.[4] To date, a wide assortment of membrane materials has been investigated and developed for gas separation applications, however, only polymer membranes have found large scale use.[5]

1.1 Polymeric Membrane Materials

Polymeric membranes are realistic alternatives to traditional gas separation techniques due to their low cost of production, ease of processing, and high degree of customizability.[6]

Currently, amorphous organic polymers account for most of the commercially available gas separation membranes.[7] Common examples include cellulose acetate which is typically utilized in natural gas sweetening processes, and polyimides which are frequently used in hydrogen recovery processes. Glassy polymers such as cellulose acetate and polyimides typically exhibit low free volume due to their rigid chain structures which restricts segmental motion. The characteristic low free volume of these polymers contributes to their high selectivity and low permeability.[8] Robeson et al. characterized the tradeoff between permeability and selectivity for the separation of small gas molecules by polymeric membranes.[9] The Robeson upper bound or limit, is the maximum performance achievable by polymeric membranes operating by a solution diffusion mechanism.[10] In addition to their limited performance, polymer membranes typically suffer from short lifetimes, and poor thermal and chemical stability. These trade-offs have resulted in the emergence of several composite membranes that utilize inorganic and hybrid fillers such as Zeolites and Metal-Organic Frameworks as means of surpassing the upper bound and improving the physical properties of polymer.

1.2 Metal-Organic Frameworks

MOFs are porous crystalline solids of organic linkers and inorganic metal nodes (or metal-cluster nodes), that make up an infinite, repeating framework of potential voids.[11] Like organic polymers, MOF precursors are selected so that the properties of the building blocks are retained in the bulk. These materials possess extremely high porosity, uniform pore sizes, and unique adsorption properties defined by their structure and composition. When compared with zeolites and other porous inorganic solids, MOFs provide several advantages including greater structural diversity and more routine synthetic procedures. In

addition, the presence of organic linkers allows for post-synthetic modification of MOF structures allowing MOFs to be finely tuned to fit a variety of applications such as gas storage[12,13], separations[14,15], catalysis[16,17], electronics[18,19], and chemical sensors[20,21]. Zeolitic Imidazole Frameworks (ZIFs) are a new class of MOFs possessing zeolite architectures formed through the self-assembly of a Zn or Co cation bridged by an imidazolate linker.[22] Zeolitic Imidazole Framework-8 (ZIF-8) represents one of the most well studied MOFs to date, formed by the coordination of four 2-methylimidazole ligands to a Zn^{2+} node, this complex assumes tetrahedral geometry and subsequently forms a ZIF with SOD topology.[23] In addition to its unique chemical and thermal stability, ZIF-8 possesses a pore aperture of 3.4 Å, a pore diameter of 11.60 Å[24], and a Langmuir surface area between 1300-1800 m^2/g which make it an promising candidate for a variety of potential applications include gas separation and sequestration.[25,26] As such, continuous efforts are being made to incorporate ZIF-8, as well as other MOFs, into composite membranes to exploit their attractive attributes.

1.3 MOF/Polymer Composite Materials

A composite is a solid comprised of two more parts which work synergistically while maintaining their own identity.[27] To date several examples of MOF composite membranes have appeared in the literature including encapsulation of polymers in MOF nanochannels, surface modification of MOFs with polymers, and most notably MOF-based mixed matrix membranes (MMMs).[28] MMMs are a class of composites membranes that feature crystals of meso- or microporous materials suspended within a polymer matrix. These membranes derive their properties from both the polymer matrix and the meso- or microporous filler, allowing for unique combinations of materials tailored to meet the demands of a variety of

applications. MOF-based MMMs provide unique advantages over more traditional fillers such as zeolites because of the high degree of compatibility between polymers and MOFs and customizability of both MOFs and polymers.[29] Size and morphology of MOF crystallites are important factors to consider when designing MOF-based membrane materials.[30] Nano-crystallites are preferred because they provide closer integration of MOF and polymer due to their relatively high surface areas. Additionally, MOF nanomaterials have shown to provide greater catalytic, ion exchange, separation, sensing and sorption performance when compared to bulk MOF materials.[31] To date, several examples exist of 0-D,[32] 1-D,[33] and 2-D,[34] MOF nanomaterials and MOF composite nanomaterials,[35] however, only a handful of examples are available demonstrating the implementation of MOF nanomaterials with controlled morphologies in a polymer matrix, i.e. MMMs.[36] Thus, designing new ways to both synthesize and incorporate MOF nanomaterials into MMMs, should lead to the enhancement of membrane technologies as a whole, and make them a more viable alternative to traditional separation techniques.

1.4 Research Outline and Thesis Statement

Through a bottom-up approach, i.e. block co-polymer (BCP) self-assembly and in-situ growth, MMMs can be templated, forming a composite with functionalized domains. Utilizing a polymer template with well-defined cylindrical pores for the in-situ growth of MOF should result in the formation of MOF nanostructures with controlled morphologies due to the effects of nanoconfinement. Additionally, a well-ordered template with defined pores allows for the sequestration of MOF nanostructures into isolated domains which should minimize the presence of MOF aggregation and microvoid formation. This methodology should be readily applicable to a wide variety of MOF and polymer systems,

making it a valuable tool for the fabrication of designer MMMs. Figure 1.1 outlines the proposed research methodology and demonstrates how a bottom up approach could be used to overcome the current shortfalls associated with MMMs and MOF thin films. To examine the feasibility of the outlined approach, track etched membranes will be used as an idealized template, since these membranes feature well-defined cylindrical pores of varying pore sizes which mimic the size and shapes achievable through BCP self-assembly. Additionally, these membranes are readily available commercially and are relatively cheap, which are both ideal conditions for this type of survey. ZIF-8 will be used as model MOF due to its well-studied nature and the comprehensive collection of synthetic schemes currently available for this material.

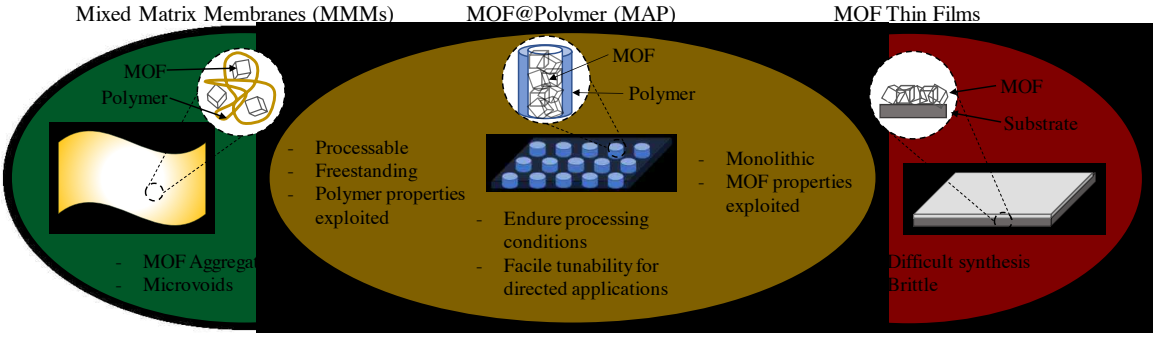

Figure 1.1. Outline of research methodology and a comparison with the current state of the field

Chapter 2.

Methodology

2.1 General Procedures

All solvents and materials were purchased from commercial sources and used as-received unless otherwise noted. All Bright-Field Transmission Electron Microscopy (BF-TEM) images and Selected Area Electron Diffraction (SAED) patterns were obtained on a JEOL-2010 equipped with a LaB_6 filament operating at 200 kV and a Gatan Orius SC1000 CCD camera. All High-Angle Annular Dark-Field Scanning Transmission Electron Microscopy (HAADF-STEM) and Energy Dispersive X-Ray Spectroscopy (EDS) were conducted on a JEOL-2010F equipped with a Field Emission Gun (FEG) operating at 200 kV, a Gatan GIF 2000 filter, and an Oxford ISIS 200 EDS system. All TEM, STEM, and EDS samples were prepared by dissolving the PCTE templates in 10mL of chloroform (Macron), the dissolved products were then cast onto 200 mesh carbon coated copper TEM grids (Ted Pella 01840-F). 2D X-Ray Diffraction (2D-XRD) patterns were obtained on a Rigaku D/Max instrument equipped with CoKα radiation source (λ = 1.78899 Å, 40kV, 30mA), a 0.8mm collimator, and a Fe filter. As synthesized samples were mounted perpendicular to the goniometer using a sample stage fabricated in house and patterns were collected for 6 hours. 2θ scans were collected using a Rigaku SmartLab Diffractometer equipped with a CuKα radiation source (λ = 1.54059 Å ,40kV, 40mA), a D/TEX detector, and a Ni filter. As synthesized samples were mounted on a quartz sample holder and patterns were collected for 2.5 hours. All Scanning Electron Microscopy (SEM) images were collected on a FEI Quanta 3D FEGSEM/FIB instrument. As synthesized samples were prepared for SEM analysis as follows; PCTE templates were cut in half with a razor

blade, and then mounted onto a glass substrate with double sided carbon tape. Samples were then coated with 10nm of aluminum using an Angstrom Engineering Åmod deposition system at a base vacuum level of <7 x 10-8 Torr and mounted to the sample stage with double sided carbon tape. Isolated SEM samples were prepared as follows; as synthesized samples were coated with 10nm of Al on one side and mounted (Al side down) onto a glass substrate using J-B Weld which cured overnight. Samples were then submerged in THF (Macron) for 10min, dried, coated with 10nm Al, and mounted to the sample stage with double sided carbon tape. BET measurements were conducted on a Micromeritics Gemini V5 2360 surface area analyzer. Samples were washed thoroughly with DI water and then dried under vacuum for 24 hours prior to analysis. All solution (300.13 MHz) ^{1}H and (75.48 MHz) ^{13}C NMR recorded on a Bruker Avance III Solution 300 spectrometer. All solution ^{1}H and ^{13}C NMR spectra were referenced internally to solvent signals, samples were prepared for NMR analysis by dissolution in $CDCl_3$ 99.8 atom % D (Sigma Aldrich). Gel Permeation Chromatography (GPC) analyses were performed on a Waters Breeze system equipped with a 2707 autosampler, a 1515 isocratic HPLC pump, and a 2414 refractive index detector. The eluent, chloroform and 0.5% (v/v) triethylamine (1mL/min), was passed through two styragel 5 μm Mix-C columns (Polymer Laboratories), calibrated with polystyrene standards (Varian). Differential scanning calorimetry (DSC) measurements were performed on a Mettler Toledo DSC STAR^{e} system with *ca.* 10 mg sample and at scan rates of 10 °C min^{-1}.

2.2 Synthesis of ZIF-8 Super- and Nanostructures

Solutions of Zn(Ac)2 • 2H2O (Alfa Aesar, 97+%) or Zn(NO3)2 • 6H2O (Alfa Aesar, 99% metals basis) in reagent grade water (BDH) and 2-MIM (Acros Organics, 99%) in 1-

Octanol (Alfa Aesar, 99%) are prepared in separate scintillation vials and stirred for one hour at room temperature. A list of concentrations for the aqueous and organic solutions can be found in Table 2.1. Afterwards, a PCTE membrane (Sterlitech Co.) with the desired pore size (Table 2.1) is gently laid onto the surface of the zinc solution with the hydrophilic side (rough side) contacting the surface of the solution. The membrane is left to soak for 24 hours after which the 2-MIM solution is gently pipetted onto the membrane. Membranes were left to react for 1 hour before being removed from the solution interface and rinsed gently with DI water, patted with a Kimwipe, and further dried under ambient conditions for 24 hours before analysis.

Table 2.1. Outline of synthetic parameters for the synthesis of ZIF-8 super- and nanostructures.

Structure	Concentration [Zn^{2+}]	Concentration [2-MIM]	Pore Size (nm)
ZIF8-30-N	0.025M (Nitrate)	1.00M	30
ZIF8-100-A	0.025M (Acetate)	2.00M	100
ZIF8-100-N	0.042M (Nitrate)	2.00M	100

2.3 Synthesis of 5-Norbornene-2,3-dicarboximide-N-methyl

A 100 mL round bottom flask was charged with 2.00 g (0.0121 mol.) of 5-Norbornene-2,3-dicarboxylic Anhydride (TCI, >97%) and 25 mL of tetrahydrofuran (Macron). 0.9866 g (1.10 mL, 0.0127 mol.) of Methylamine (Alfa Aesar, 40% w/w aq. soln.) is added to the flask dropwise and allowed to stir, resulting in the formation of a white precipitant. After which ~10mg of p-Toluene sulfonic acid monohydrate (Alfa Aesar, 98.5+%) in 2 mL of methanol (Macron) is added to the flask, the solution is then refluxed at 70 °C for 24 hours. The product was isolated by distillation, and re-dissolved in dichloromethane, washed twice with a 1M bicarbonate solution, then twice with a brine solution, dried over Na_2SO_4, and filtered. The product was then recrystallized from methanol to give white needle-like crystals (1.38 g, 69 y%). ^{1}H NMR (300.13 MHz, $CDCl_3$): δ (ppm) = 1.53~1.60 (d, 1H),

1.72~1.75 (d, 1H), 2.82 (s, 3H), 3.26~3.28 (d, 4H), 6.09 (t, 2H). ^{13}C NMR (75.48 MHz, $CDCl_3$): δ (ppm) = 24.354, 44.939, 46.091, 52.336, 134.569, 177.940.

2.4 Synthesis of Polynorbornene-b-poly(5-norbornene-2,3-dicarboximide-N-methyl)

Grubbs 3rd generation catalyst (G3) was synthesized as described by Tae-Lim et al.[37] 125 mL Erlenmeyer flask with a 19/22 ground glass joint was charged with 1.4216 g (0.015 mol.) of Bicyclo[2.2.1]hept-2-ene (Sigma Aldrich, 99%) and 75 mL of dichloromethane (EMD Millipore). The solution was cooled to -20 °C at which time 16 mg (0.018 mmol.) of G3 was added to the flask in a minimal amount of DCM; addition of G3 results in a rapid color change of the solution from green to orange indicating initiation of the polymerization. After two minutes 0.7108 g (0.0039 mol.) of 5-Norbornene-2,3-dicarboximide-N-methyl is added to the reaction flask in a minimal amount of DCM, the flask is then quickly transferred to a water bath preset to 40 °C and left for 1.5 hours. The polymerization is terminated by the addition of 0.5 mL of ethyl vinyl ether (Alfa Aesar, 99%). The polymer is isolated by precipitation into methanol (1.59 g, 90 %). ^{1}H NMR (300.13 MHz, $CDCl_3$): δ (ppm) = 1.04 (broad, m), 1.35 (broad, s), 1.81 (broad, m), 2.43 (broad, s), 2.79 (broad, s), 2.96 (broad, s), 3.22 (broad, m), 5.21~5.19 (d, 2H, *cis*), 5.34 (s, 2H, *trans*), 5.64 (broad, s, 2H, *cis*), 5.72 (s, 2H, *trans*).

Chapter 3

Results and Discussion

3.1 1-D ZIF-8 Super- and Nanostructures

The following section describes the synthesis and characterization of 1-Dimensional (1-D) ZIF-8 nanorods, nanotubes, and nanowires through interfacial synthesis templated by nanoporous polymer membranes. It should be noted that the contents of this chapter have been previously published/reported in Angewandte Chemie.[38] Initially inspired by the concept of solution contra-diffusion,[39,40] interfacial synthesis provides a unique mechanism for the directed self-assembly of MOF crystal growth.[41,42]

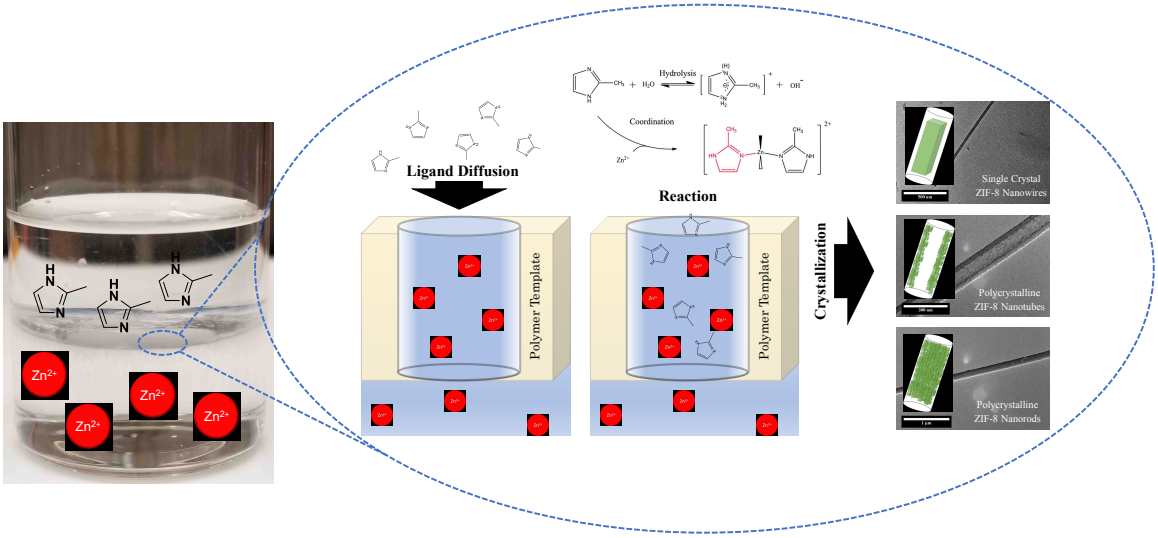

Figure 3.1. Scheme outlining the synthesis of the ZIF-8 super- and nanostructures.

A full synthetic scheme is provided in Chapter 2.2 of this manuscript and Figure 3.1 further outlines the synthetic approach. In principle, polycarbonate track-etched (PCTE) membranes (Sterlitech Co.) were supported between an aqueous solution of the metal precursor and an organic solution of the ligand and left to react for one hour before being removed from the reaction medium. PCTE membranes were chosen as templates due to

their ease of accessibility, varying pore sizes, and well-defined pore dimensions. To date, several examples of membrane templated synthesis of nanostructures have been reported in the literature,[43–45] however, this work represents the first example of membrane templated self-assembly of MOF super- and nanostructures.

A thorough examination of the ZIF-8 nanostructures was accomplished through a combination of X-Ray crystallography and electron microscopy techniques. Beginning with 2D-X-Ray Diffraction (2D-XRD), integrated XRD patterns were generated by integration of the 2D-XRD patterns from 221.41° to 490.42° (β), a scan from a blank membrane was used to subtract the background signal, the resulting patterns are shown in Figure 3.2.

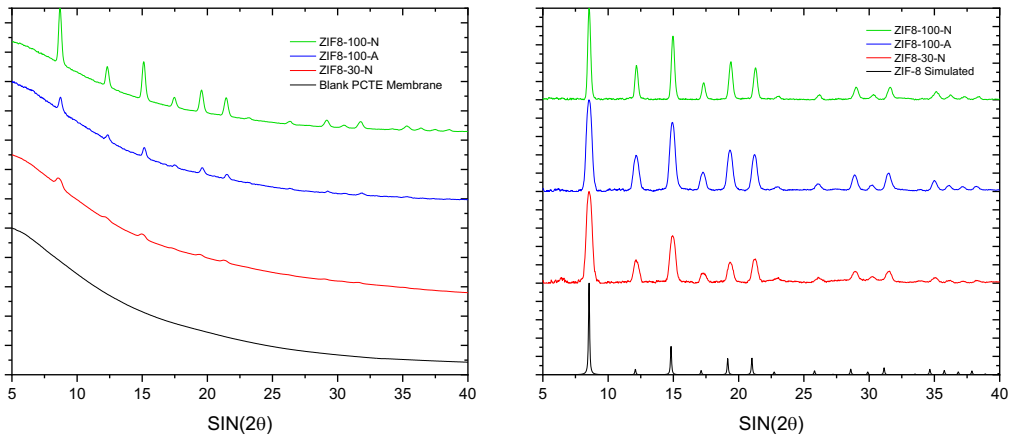

Figure 3.2. (Left) 2D-XRD patterns for all three representative samples, as collected. (Right) Background subtracted 2D-XRD patterns and simulated pattern for ZIF-8 single crystal.

The scattering signals of all three samples are consistent with simulated powder XRD pattern of ZIF-8 single crystal, suggesting the presence of ZIF-8 crystallites within the film. It should be noted that the relative peak intensities of the (110) and (200) Bragg planes are inconsistent with the observed intensities of the simulated pattern, which is a typical feature of samples with preferred orientation. Oriented growth of ZIF-8 crystals has been

previously demonstrated, through crystallographic preferred orientation (CPO) analyses.[46,47] The CPO indices were calculated using the integrated intensities of the (110), (200), and (211) Bragg planes for each of the representative sample types using Equation 3.1.

$$\mathrm{CPO}_{(002)/(011)} = \left[\left(\frac{I_{(002)}}{I_{(011)}}\right)_{Sample} - \left(\frac{I_{(002)}}{I_{(011)}}\right)_{Standard}\right] / \left(\frac{I_{(002)}}{I_{(011)}}\right)_{Standard} \quad \text{Eq. 3.1}$$

Table 3.1. Crystallographic preferred orientation (CPO) indices for the three representative sample types.

Structure	$CPO_{(002)/(011)}$	$CPO_{(002)/(112)}$
ZIF8-30-N	3.16	1.33
ZIF8-100-A	5.99	1.59
ZIF8-100-N	6.21	1.88

Table 3.1 lists the calculated $CPO_{(200)/(110)}$ indices for ZIF8-30-N, ZIF8-100-A, and ZIF8-100-N which are 3.16, 5.99, and 6.21 respectively. The $CPO_{(200)/(110)}$ indices suggest a preferential orientation of the {100} planes parallel to the surface of the pore walls, or perpendicular to the surface of the membrane. The relatively low CPO values, typically well above 50.00 for a well aligned sample, are likely due to the misalignment of the pores caused by the track etching process and the presence of residual randomly oriented crystallites present on the surface of the film, visible by Scanning Electron Microscopy (SEM).

Electron microscopy techniques, SEM and transmission electron microscopy (TEM), allow for a better characterization of the template surface and, after isolation, the ZIF-8 super- and nanostructures. By SEM there is clear evidence of pore filling on both surfaces of the PCTE membranes with 100nm pores (Figure 3.3), which would suggest complete pore filling, however pore filling is not clearly observed on either surface of the 30nm

PCTE membranes, indicating partial or no pore filling. The hydrophilic and hydrophobic surfaces of all of the membranes contain surface materials, which were impossible to remove completely without damaging the films.

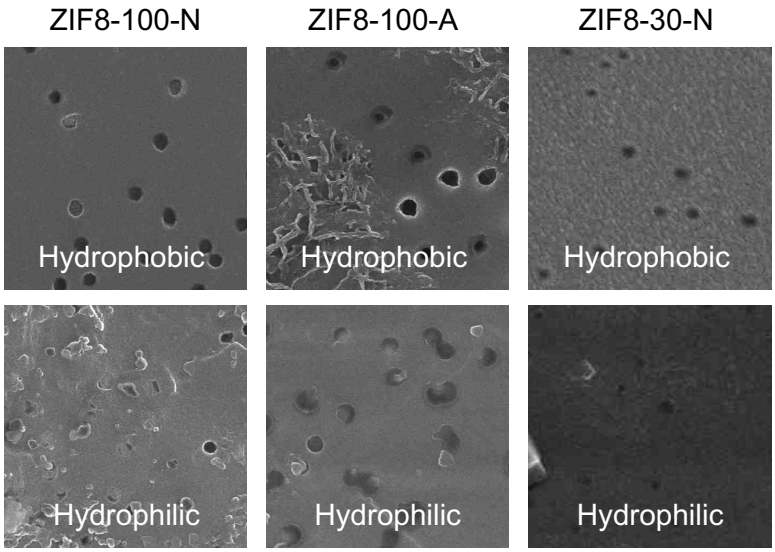

Figure 3.3. SEM images of template surfaces. The hydrophobic surface of the membrane positioned towards organic phase during synthesis. (From left to right) ZIF8-100-N, ZIF8-100-A, and ZIF8-30-N.

Structures were isolated from the PCTE membranes as described in Chapter 2.1 and characterized by bright-field transmission electron microscopy (BF-TEM), images from each of the representative samples are shown in Figures 3.4, 3.5, and 3.6. From the 100 nm PCTE templates two distinct architectures are observed by TEM, namely solid nanorods (ZIF8-100-N, Figure 3.5) and hollow nanotubes (ZIF8-100-A, Figure 3.4) with average lengths of 6 μm, consistent with the template thickness. Upon closer examination, the superstructures appear to be comprised of intergrown ZIF-8 nanocrystallites, which is confirmed by the selected area electron diffraction (SAED), shown in Figure 3.7.

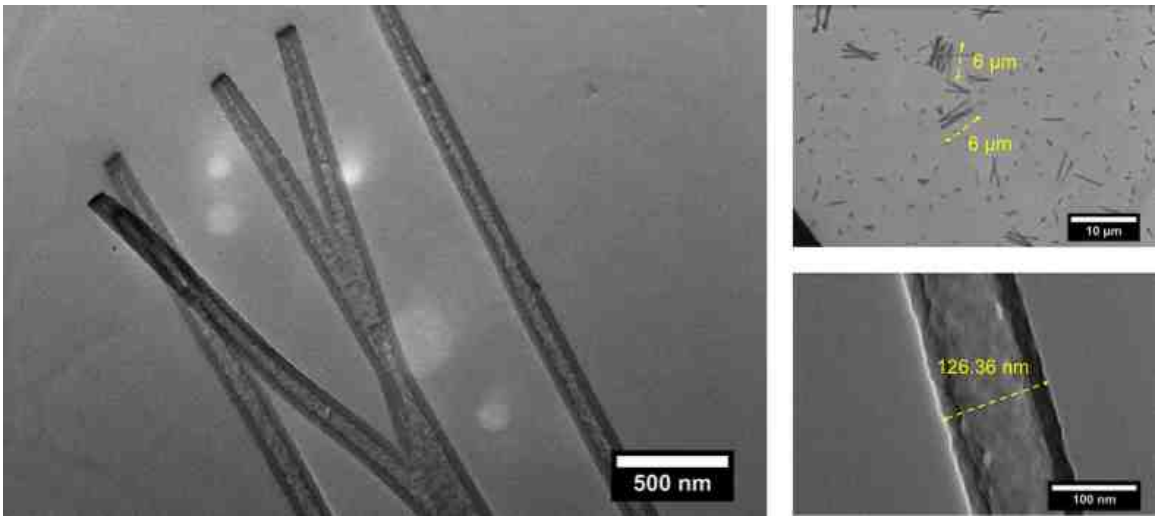

Figure 3.4. (Left) BF-TEM image of ZIF-8 nanotubes (ZIF8-100-A). (Top-Right) Image depicting an average 6 µm length for the ZIF-8 nanotubes. (Bottom-Right) Image depicting the average width of the ZIF-8 nanotubes.

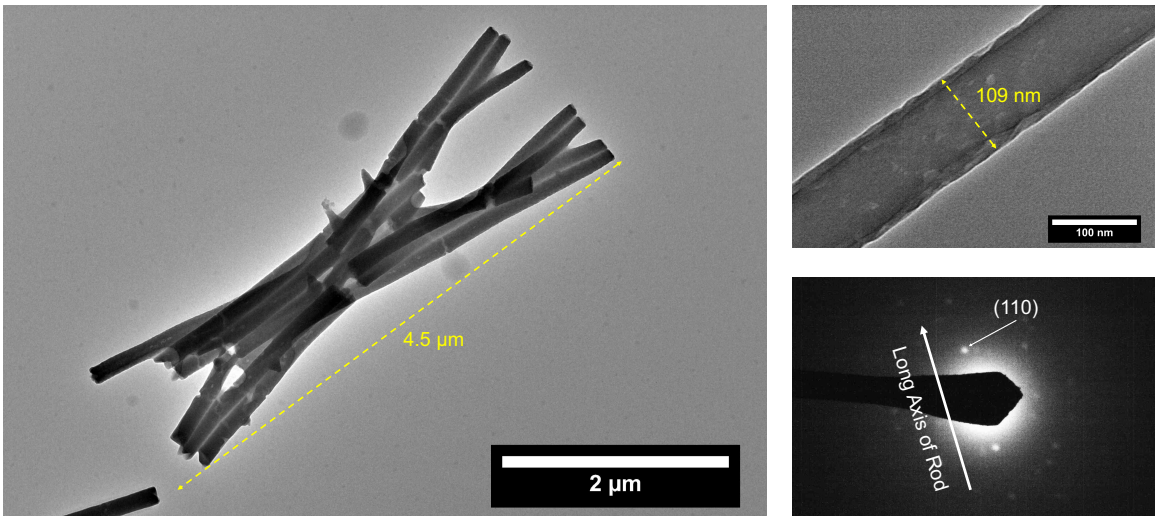

Figure 3.5. (Left) BF-TEM image of ZIF-8 nanorods (ZIF8-100-N). (Top-Right) Image depicting an average width of the ZIF-8 nanotubes. (Bottom-Right) SAED of a single ZIF-8 nanorod.

It should be noted that the SAED patterns are collected from groups of rods or tubes owing to the difficulty in selectively analyzing one single nanostructure caused by the known intrinsic electron beam sensitivity of ZIF-8.[48]

On the other hand, products isolated from the PCTE membranes featuring 30 nm pores exhibited widths consistent with diameter of the pores while lengths were limited to an average of 2 μm (Figure 3.6), explaining the lack of observable pore filling at the membrane surface. A closer examination reveals cubic facets at the ends of the nanowires, angled at ca. 408, are consistent with those of {110} planes. SAED images collected from ZIF8-30-N display single-crystal patterns with the {110} planes normal to the nanowire long axis (Figure 3.7).

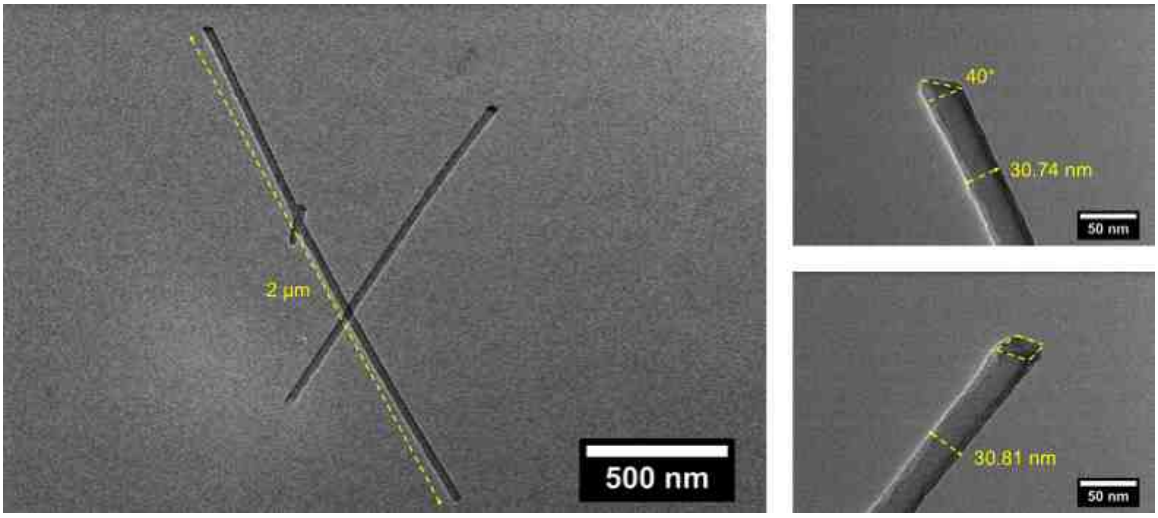

Figure 3.6. (Left) BF-TEM image of ZIF-8 nanowires (ZIF8-30-N). (Top-Right) and (Bottom-Right) Images depicting an average width of the ZIF-8 nanowires as well as cubic faceted wire caps.

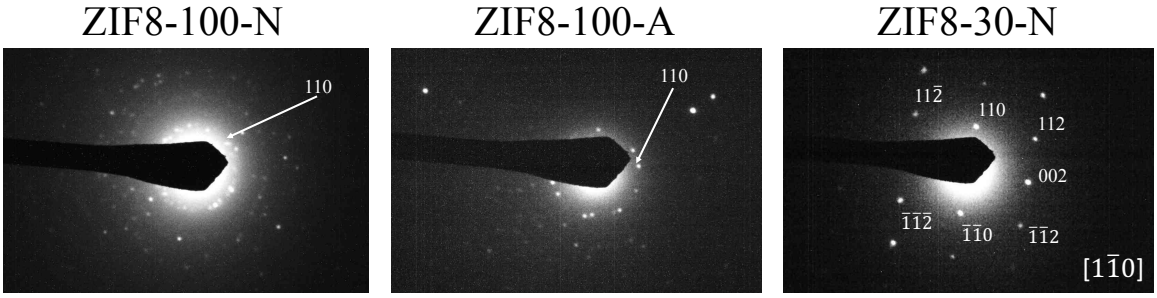

Figure 3.7. SAED patterns for the representative samples. Samples were calibrated using a silicon standard.

A more extensive X-Ray analyses was conducted on the ZIF8-30-N membranes to confirm that the ensemble average was consistent with the observations made by TEM. The 2θ-XRD profiles (Figure 3.8) match closely to those taken by transmission mode 2D-XRD and the ZIF-8 simulated pattern. A fitting by Rietveld refinement (Figure 3.8) of the 2θ scan revealed the presence of two discreet crystallite sizes (Table 3.2),[49] one between 20 and 40 nm the other well over 500 nm, these results are consistent with the observations made by SEM and TEM. It could be argued that the spectral feature is not a convolution of two Voigt profiles but rather is more Lorentzian in character, however, profile fitting of the {100} peak of ZIF8-30-N (Figure 3.9) to a pure Lorentzian function does not yield conclusive results.

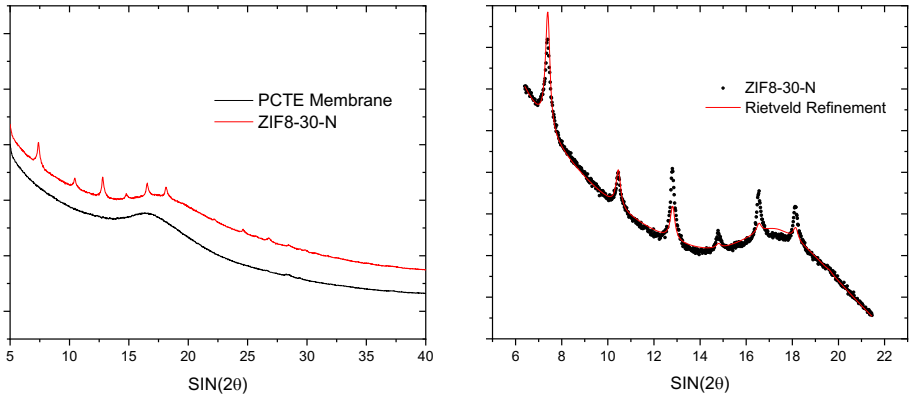

Figure 3.8. (Left) Uncorrected 2θ-XRD scan for ZIF8-30-N and a blank PCTE membrane. (Right) Rietveld refinement for ZIF8-30-N.

Table 3.2. Tabulated results from Rietveld refinement.

Angle(°)	d(Å)	Centroid(°)	Centroid(Å)	FWHM(°)	XS(Å)	(h k l)
7.3895 (0.0035)	11.95357 (0.01117)	7.3895	11.95357	0.458 (0.011)	204	(110)
7.3842 (0.0016)	11.96211 (0.00509)	7.3842	11.96211	0.137 (0.004)	>5000	(110)
10.4390 (0.0031)	8.46746 (0.00498)	10.4390	8.46746	0.128 (0.007)	>5000	(200)
10.4730 (0.0093)	8.44006 (0.01490)	10.4730	8.44006	0.405 (0.018)	241	(200)
12.7882 (0.0015)	6.91676 (0.00166)	12.7882	6.91676	0.119 (0.004)	>5000	(211)
12.8171 (0.0034)	6.90124 (0.00361)	12.8171	6.90124	0.385 (0.007)	258	(211)
14.7697 (0.0045)	5.99295 (0.00361)	14.7697	5.99295	0.040 (0.011)	>5000	(220)
14.7902 (0.0061)	5.98469 (0.00493)	14.7902	5.98469	0.278 (0.012)	433	(220)
16.5204 (0.0029)	5.36159 (0.00185)	16.5204	5.36159	0.133 (0.007)	>5000	(310)
16.5729 (0.0147)	5.34475 (0.00943)	16.5729	5.34475	0.386 (0.026)	259	(310)
18.2298 (0.0527)	4.86251 (0.02787)	18.2298	4.86251	0.625 (0.054)	142	(222)
18.1163 (0.0029)	4.89272 (0.00155)	18.1163	4.89272	0.166 (0.008)	>5000	(222)

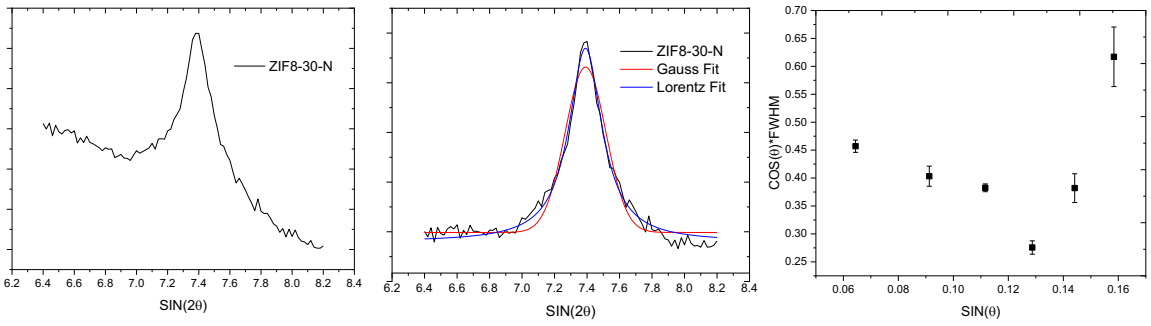

Figure 3.9. (Left) {110} peak for ZIF8-30-N. (Middle) Gauss and Lorentz Fitting of {110} peak after background correction. (Right) Williamson-Hall analysis for ZIF8-30-N.

Additionally, Williamson–Hall analysis predicts average crystallite size to be about 27 nm, which is consistent with the width of the nanowires (Figure 3.9).[50] Analysis of the signals using March–Dollase approach results in a March parameter of 0.55 indicating preferred orientation of the {110} planes parallel to the film surface, confirming our assignments by SAED.[51] These results suggest the observed ZIF-8 nanowires are single crystals with large aspect ratios and a preferred orientation with the {110} planes roughly perpendicular to the long axis of the nanowire.

The formation of continuous super- and nanostructures can be attributed to several factors. Based on the specifications from Sterlitech, the PCTE membranes are coated with a thin layer of poly(N-vinyl- pyrrolidinone) (PVP) to impart hydrophilicity. It has previously been demonstrated that PVP acts as a molecular anchor for the nucleation and growth of ZIF-8.[52] Initially, when the Zn ions and 2-MIM mix inside the 100 nm pores during the interfacial synthesis, PVP anchors for the initially formed ZIF-8 seed crystals to the surface of the pore wall, resulting in growth from the pore wall inward, gradually forming hollow tubes and solid rods. Interestingly, the formation of tube like structures suggests that the reaction is terminated by capping mechanism which prevents the further diffusion of reactants through the pores. It is assumed that the zinc concentration is constant at the beginning of the reaction due to the prolonged soak time which allows the concentration within the pore to eventually reach the solution concentration. Upon addition of the organic solution the reaction proceeds at a rapid rate at the interface of the two solutions, and as 2-MIM diffuses progressively throughout the pores the reaction proceeds at rate relatively slower than at the solution interface. Eventually the interface reaction outcompetes the reaction within the pores resulting in a plug at the solution interface, which

can be observed at the nanotube ends (Figure 3.4 and Figure 3.3), terminating the reaction. Additionally, the slower crystal growth rate for $Zn(Ac)_2$ when compared to $Zn(NO_3)_2$, due to the relatively stronger metal-ligand interactions, would suggest even larger discrepancies in their relative growth rates at the solution interface and along the pores resulting in capping long before solid rod formation. This is further confirmed by varying the $Zn(Ac)_2$ concentration in solution while maintaining the concentration of 2-MIM in the organic phase constant (Figure 3.10). At lower concentrations discrete networks of nano-crystallites can be observed and as the concentration is raised nanotubes and then nanorods can be observed as expected.

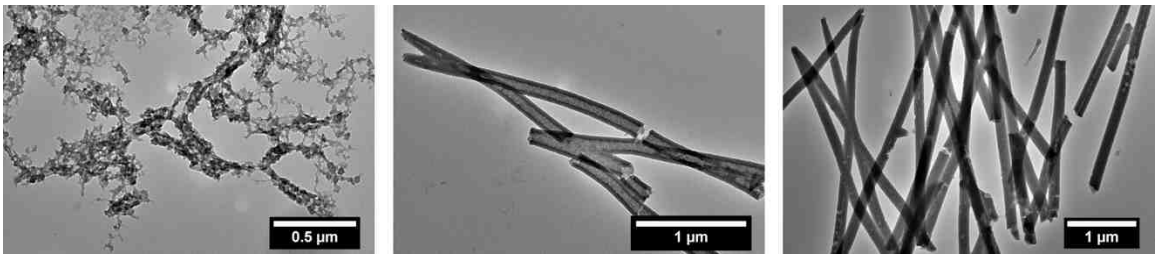

Figure 3.10. Examination of the effects of metal precursor concentration on structure. (From left to right) 0.008 M, 0.025 M, and 0.042 M $Zn(Ac)_2$.

The appearance of single crystal nanostructures 30 nm is suspected to be caused by a separate growth mechanism that is attributed to the effects of nanoconfinement caused by the reduced pore size. Under nanoconfinement the ZIF- 8 seed crystals are not stable owing to the competing surface to volume free energies, according to an Ostwald ripening mechanism.[53] As a result, a fast re-dissolution/recrystallization processes eventually leads to the formation of one stable single crystal of the largest size. It has been previously demonstrated that the {100} faces of ZIF-8 are initially the fastest growing facets, leading to cubic seed crystals, and then the growth of 12 {110} faces dominates, eventually resulting in truncated rhombic dodecahedron single crystals.[54] The spatial confinement in

two dimensions, created by the pore walls, leads to the fastest-growing {110} faces along the only unrestricted direction, that is, the long axis of the pore, resulting in the observed preferred crystal orientation.

To determine the porosity of the ZIF-8 nanostructures within the PCTE templates the PCTE membranes were subjected to Brunauer–Emmett–Teller (BET) surface area analyses and the results are summarized in Table 3.3.

Table 3.3. BET surface area measurements for the three representative samples.

	PCTE (100 nm)	ZIF8-100-N	ZIF8-100-A	PCTE (30 nm)	ZIF8-30-N
SA_{BET} (m^2/g) [a]	1.263	2.671	0.4029	0.4841	0.66
SA_{ZIF} (m^2/g) [b]	-	379.8	N.A.	-	1025

The surface areas of the 100 nm and 30 nm templates are estimated to be 1.263 m^2/g and 0.4841m^2/g respectively and are in general agreement with the manufacture specifications. After incorporation of the ZIF-8 super- and nanostructures the surface areas of membrane samples are estimated to be 2.671 m^2/g, 0.4029 m^2/g, and 0.6600 m^2/g, for ZIF8-30-N, ZIF8-100-A, and ZIF8-100-N respectively. Both ZIF8-100-N and ZIF8-30-N show increased surface area relative to the blank PCTE membranes confirming their nanoporous nature and pore accessibility. The surface areas of ZIF8-100-N and ZIF8-30-N were calculated to be 379.8 m^2/g and 1025 m^2/g respectively, based on the average dimensions obtained by TEM and a ZIF-8 bulk density of 0.35 g/cm^3. These estimates are in good agreement with the experimental results, particularly for ZIF8-30-N. On the other hand, ZIF8- 100-A membranes show a decreased surface area from 1.263 m^2/g to 0.4029 m^2/g, suggesting the ZIF-8 nanotubes either are non-porous or have inaccessible pores. The apparent discrepancies in BET surface areas are likely caused by the differences in ZIF- 8

crystal quality between the three samples. ZIF8-100-A possesses the worst crystal quality since the acetate ligand slows the reaction rate relative to nitrate anion, leading to premature and underdeveloped crystallites, while ZIF8-30-N and ZIF8-100-N utilize the nitrate anion, resulting in higher crystal quality and higher porosity, with ZIF8-30-N being the most crystalline and the most porous.

Chapter 4

Conclusions

4.1 Conclusions and Future Outlook

In summary, templated interfacial synthesis has proven a useful tool for the formation of MOF nanostructures with controlled morphologies and orientations. This approach has shed light on the effects of surface functionalization and nanoconfinement on the MOF growth mechanism. This technique has clearly demonstrated that it is possible to incorporate well-defined, oriented MOF super- and nanostructures in porous polymer templates. These designer MMMs possess accessible nanoporous surfaces intrinsic to the MOFs embedded in them, rendering them potentially useful in membrane separation processes.

Currently attempts to produced additional MOF nanostructures have proven productive, three additional MOF systems have been attempted (ZIF-67, ZIF-68, and ZIF-11) and these attempts have produced nanostructures with similar morphologies as seen in ZIF-8 (Figure 4.1). However, further studies need to be performed in order to confirm the crystallinity and composition of these materials.

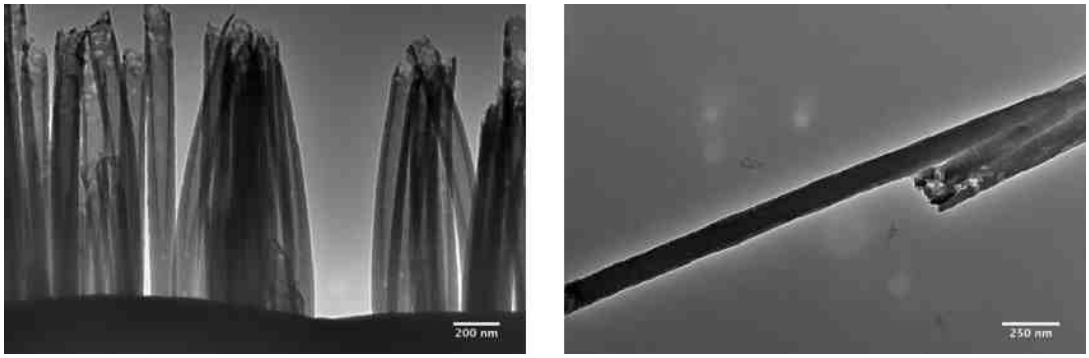

Figure 4.1. (Left) Nanostructures produced from $Zn(NO_3)_2$ and Imidazole (ZIF-6). (Right) Nanostructures produced from $Zn(NO_3)_2$ and Benzimidazole (ZIF-11).

These works have shed some light on some of the necessary conditions for the formation of templated nanostructures. Mainly, that the ligand should not only be soluble in the organic phase, but, should also be soluble in the aqueous phase which will promote its diffusion through the pores of the polymer template. One way we have been able to accomplish this is through the use of bases such as TEA as described by Kim et al.,[55] however, TEA is incompatible with the PCTE membranes, so this approach is limited.

Additionally, progress is currently being made toward the development of new polymeric materials for the fabrication of block co-polymer asymmetric self-assembled membranes (BCP-ASMs) that will be utilized for the direct self-assembly of MOF nanostructures. These unique membrane materials take advantage of the entropy driven self-assembly of block co-polymers with the industrially relevant asymmetric membrane production process, leading to the formation of membrane materials with a well ordered nanoporous surface layer and a dense skin layer.[56] These asymmetric membranes are preferred over traditional dense films due to the relatively thin selective layer which maximizes the flux or the flow of material across the membrane while providing a dense support layer which affords increased integrity to the films preventing membrane rupture.[57]

Outlined below is a synthetic scheme for a di-block copolymer and its constituents (Figure 4.2) which will serve as an ideal foundation for this exploratory study. Ring-opening metathesis polymerization was chosen because of its controlled nature, in addition to stability of Grubbs catalyst which allows for the polymerization to take place under mild conditions and in the presence of air.[58] A norbornene derived block co-polymer is an idealized system, since the Diels-Alder reaction of cyclopentadiene with a vinyl functionalized electron withdrawing (EWG) or electron donating group (EDG) allows for

easy and rapid synthesis of a variety of functionalized norbornene monomers. Additionally, hydrogenation of the poly(norbornene) backbone leads to a highly crystalline polymeric material which would be favored due to the relatively low free volume.[59]

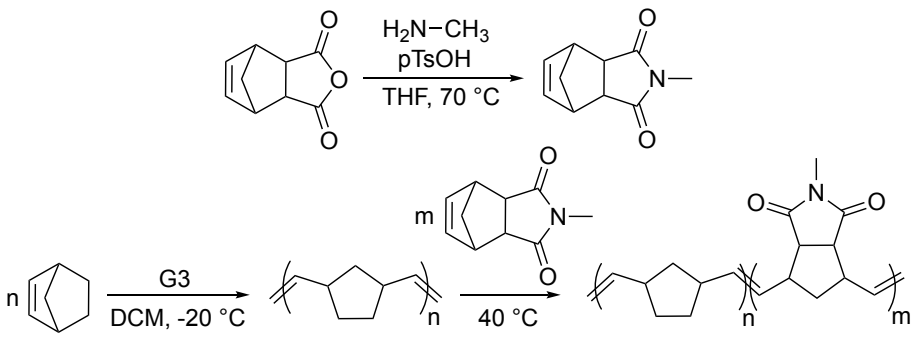

Figure 4.2. Outline of synthetic for the preparation of a di-block co-polymer which will be used in the fabrication of a BCP-ASM

The targeted monomer for the minority block was 5-Norbornene-2,3-dicarboximide-N-methyl, to be referred to as NBI, features functionality similar to the pyrrolidone ring in PVP and should exhibit similar properties with regards to the anchoring and stabilization of ZIF-8 nucleation in the pores of the membrane. NBI was synthesized as described in Chapter 2.3. Figure 4.3 includes the ^{1}H NMR and ^{13}C NMR which indicate the formation of the desired compound. It should be noted that the NMR spectra include ^{13}C satellite peaks, which are not to be confused with trace impurities.

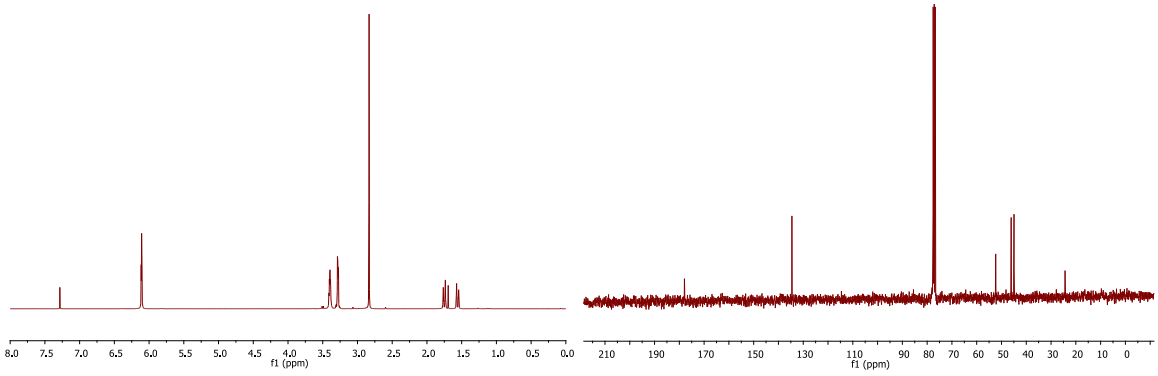

Figure 4.3. (Left) ^{1}H NMR spectra for NBI. (Right) ^{13}C NMR spectra for NBI.

A kinetics study was conducted on the ROMP of NBI to study the livingness, i.e. lack of termination and chain transfer events, of the polymerization utilizing the procedure outlined by Tae-Lim et al.[37] Grubbs third generation catalyst was used because of its rapid initiation rates, which outcompete the fast propagation rates seen in norbornene.[60] Included in Figures 4.4 and 4.5 are the ^{1}H NMR spectra and GPC traces from this study and a summary of the relevant kinetics data can be found in Table 4.1.

Table 4.1. Summary of NBI polymerization kinetics.

Reaction Time (Min)	Retention Time (Min)	Mw (Da)	Mn (Da)	Dispersity	% Monomer Conversion
2	16.142	2732	2995	1.096	0.1304
5	15.559	5110	5110	1.095	0.2453
10	15.111	8611	8611	1.264	0.3622
20	14.695	11829	11829	1.147	0.4895
30	14.505	14635	14635	1.143	0.6076

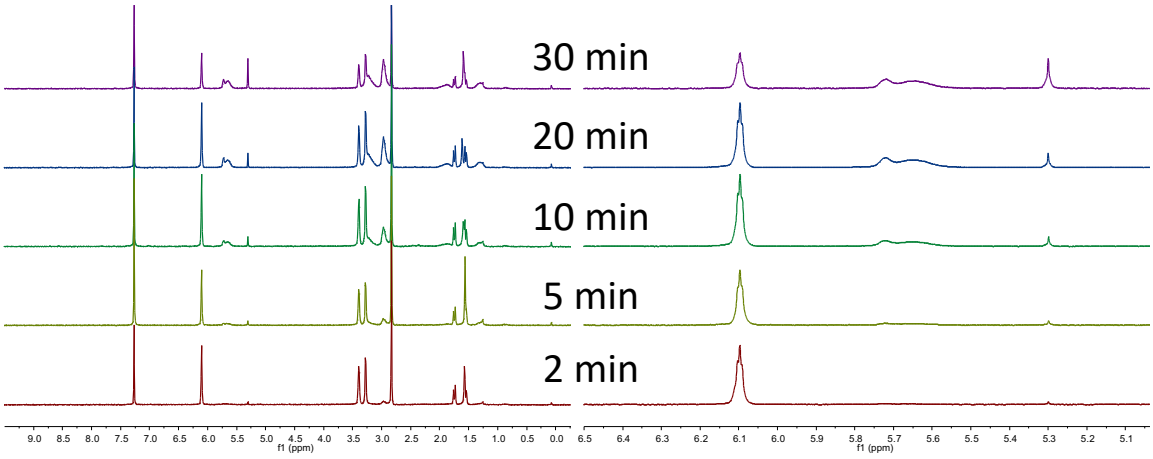

Figure 4.4. (Left) ^{1}H NMR of the polymerization kinetics for NBI, time indicates reaction progress. (Right) Region of NMR spectra, depicting vinyl protons of the polymer backbone and diene protons on NBI, used for the determination of percent monomer conversion.

The polymerization of NBI did not proceed as reported, propagation rates at room temperature were much slower than expected, possibly due to the presence of the endo-isomer of NBI.[61] Further analysis by NMR, with experiments such as NOE, should be able

to elucidate the exact structure and confirm if this is the case. GPC traces show a gradual shift of a single narrow peak from longer to shorter retention times, indicating the gradual extension of the polymer chain ends, consistent with a chain growth mechanism. The sample taken at 10 minutes displays uncharacteristic peak broadening which may be attributed to poor sampling of the reaction mixture. Plotting the number average molecular weight (M_n) versus percent monomer conversion produces a linear trend indicating a living polymerization with first order kinetics (Figure 4.5). These results suggest that NBI can be utilized in the synthesis of a di-block co-polymer, however, to minimize the possibility of chain termination events and chain transfer processes which are more likely to occur as the at longer reaction times, higher concentrations of the monomer and higher temperatures will be employed in the polymerization of NBI allowing for more precise control over the relative block lengths and their composition.

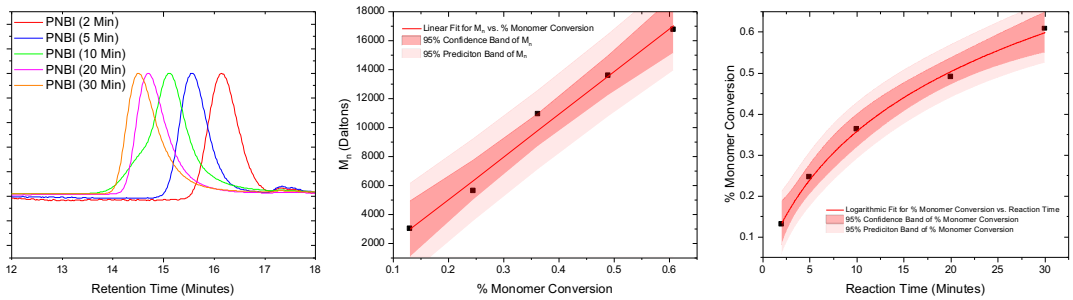

Figure 4.5. (Left) GPC traces for the polymerization of NBI, time indicates reaction progress. (Middle) Plot of M_n vs. percent monomer conversion. (Right) percent monomer conversion vs. time.

A full synthetic protocol is featured in Chapter 2.4 regarding the synthesis of poly(norbornene)-b-poly(5-Norbornene-2,3-dicarboximide-N-methyl), herein referred to as PNB-b-PNBI. To insure complete consumption of the first monomer before addition of the second monomer, limiting the possibility of mixing of the individual blocks, norbornene was polymerized first at low temperature as reported by Tae-Lim et al.,[37] since

it exhibits significantly faster initiation and propagation rates than NBI, leading to a much lower dispersity of the di-block polymer and better block compositions. A polymer with 20 w% NBI was targeted, and one equivalent excess of NBI was added to the reaction vessel to increase the relative reaction rates.

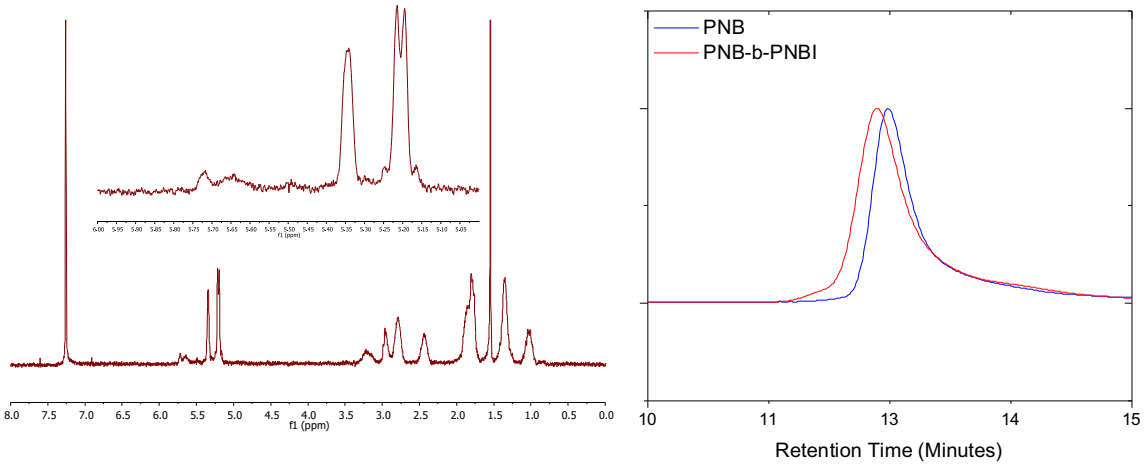

Figure 4.6. (Left) ^{1}H NMR spectra for PNB-b-PNBI, inset displays region used for determination of polymer weight fractions. (Right) GPC traces for the first block, PNB homopolymer, and PNB-b-PNBI di-block co-polymer.

Included in Figure 4.6 are the ^{1}H NMR spectra and GPC traces for PNB-b-PNBI. Examination of the proton NMR spectra indicates a minority block weight fraction of ~25% which is slightly larger than the target weight fraction, which can be explained by the relatively long tails in the GPC traces indicating the presence of poly(norbornene) homopolymer which that did not undergo chain extension. GPC traces show a complete shift of the main polymeric peak to shorter retention times with a M_n of 144,807 Da and dispersity of 1.18 for the first block and a M_n of 164,698 Da and a dispersity of 1.31 for the di-block. The slight broadening in the dispersity suggest that there is a delayed crossover upon addition of NBI which results in some chains undergoing chain extension before others.

Analysis of PNB-b-PNBI by DSC shows one distinct glass transition temperature (T_g) peak which is consistent with the T_g for PNB (Figure 4.7). There is a slight depression in the T_g from 47.11 °C to 37.70 °C which is expected considering the decreased domain size of PNB in the di-block co-polymer compared to the PNB homopolymer.[62] The PNBI homopolymer shows no T_g in the range measured and no additional T_g is observed in the PNB-b-PNBI.

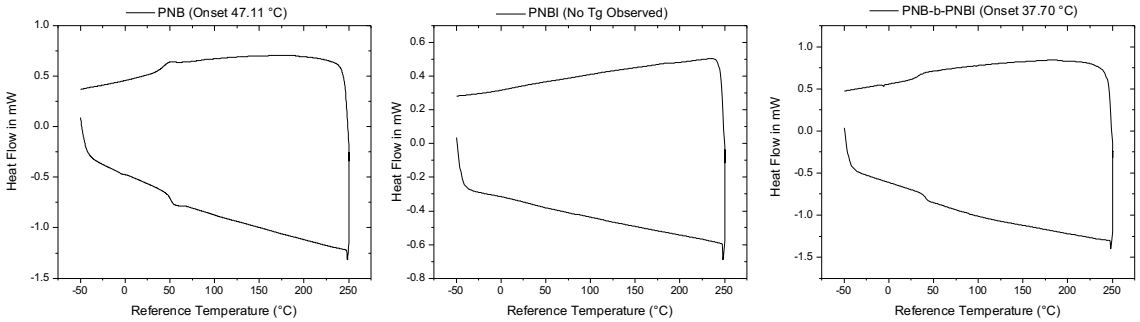

Figure 4.7. DSC isotherms for PNB (Left), PNBI (Middle) and PNB-b-PNBI (Right)

These results together suggest the formation of a new di-block co-polymer, PNB-b-PNBI, however, limited studies have been made utilizing this designer polymer for the fabrication of a BCP-ASM. Currently, steps are being taken to determine the optimized conditions which promote the self-assembly of PNB-b-PNBI, furthermore, hydrogenation of the polymer backbone may help to promote the ASM fabrication process. Once a BCP-ASM has been produced steps will be taken to incorporate MOF into the newly formed templates.

References

(1) Oak Ridge National Laboratory. Materials for Separation Technologies: Energy and Emission Reduction Opportunities. **2005**.

(2) Sholl, D. S.; Lively, R. P. Seven Chemical Separations to Change the World. *Nature* **2016**, *532* (7600), 435–437.

(3) Gin, D. L.; Noble, R. D. Designing the Next Generation of Chemical Separation Membranes. *Science (80-.).* **2011**, *332* (6030), 674 LP-676.

(4) Galizia, M.; Chi, W. S.; Smith, Z. P.; Merkel, T. C.; Baker, R. W.; Freeman, B. D. 50th Anniversary Perspective: Polymers and Mixed Matrix Membranes for Gas and Vapor Separation: A Review and Prospective Opportunities. *Macromolecules* **2017**, *50* (20), 7809–7843.

(5) Baker, R. W.; Low, B. T. Gas Separation Membrane Materials: A Perspective. *Macromolecules* **2014**, *47* (20), 6999–7013.

(6) Basu, S.; Khan, A. L.; Cano-Odena, A.; Liu, C.; Vankelecom, I. F. J. Membrane-Based Technologies for Biogas Separations. *Chem. Soc. Rev.* **2010**, *39* (2), 750–768.

(7) Robeson, L. M. Polymer Membranes for Gas Separation. *Curr. Opin. Solid State Mater. Sci.* **1999**, *4* (6), 549–552.

(8) Alexander Stern, S. Polymers for Gas Separations: The next Decade. *J. Memb. Sci.* **1994**, *94* (1), 1–65.

(9) Robeson, L. M. Correlation of Separation Factor versus Permeability for

Polymeric Membranes. *J. Memb. Sci.* **1991**, *62* (2), 165–185.

(10) Robeson, L. M. The Upper Bound Revisited. *J. Memb. Sci.* **2008**, *320* (1), 390–400.

(11) Batten, S. R.; Champness, N. R.; Chen, X.-M.; Garcia-Martinez, J.; Kitagawa, S.; Öhrström, L.; O'Keeffe, M.; Paik Suh, M.; Reedijk, J. Terminology of Metal–Organic Frameworks and Coordination Polymers (IUPAC Recommendations 2013). *Pure Appl. Chem.* **2013**, *85* (8), 1715–1724.

(12) Sumida, K.; Rogow, D. L.; Mason, J. A.; McDonald, T. M.; Bloch, E. D.; Herm, Z. R.; Bae, T.-H.; Long, J. R. Carbon Dioxide Capture in Metal–Organic Frameworks. *Chem. Rev.* **2012**, *112* (2), 724–781.

(13) Jiang, J.; Furukawa, H.; Zhang, Y.-B.; Yaghi, O. M. High Methane Storage Working Capacity in Metal–Organic Frameworks with Acrylate Links. *J. Am. Chem. Soc.* **2016**, *138* (32), 10244–10251.

(14) Denny Jr., M. S.; Moreton, J. C.; Benz, L.; Cohen, S. M. Metal–Organic Frameworks for Membrane-Based Separations. *Nat. Rev. Mater.* **2016**, *1*, 16078.

(15) Vellingiri, K.; Deep, A.; Kim, K.-H. Metal–Organic Frameworks as a Potential Platform for Selective Treatment of Gaseous Sulfur Compounds. *ACS Appl. Mater. Interfaces* **2016**, *8* (44), 29835–29857.

(16) Lee, J.; Farha, O. K.; Roberts, J.; Scheidt, K. A.; Nguyen, S. T.; Hupp, J. T. Metal-Organic Framework Materials as Catalysts. *Chem. Soc. Rev.* **2009**, *38* (5), 1450–1459.

(17) Kim, C. R.; Uemura, T.; Kitagawa, S. Inorganic Nanoparticles in Porous Coordination Polymers. *Chem. Soc. Rev.* **2016**, *45* (14), 3828–3845.

(18) Stavila, V.; Talin, A. A.; Allendorf, M. D. MOF-Based Electronic and Opto-Electronic Devices. *Chem. Soc. Rev.* **2014**, *43* (16), 5994–6010.

(19) So, M. C.; Wiederrecht, G. P.; Mondloch, J. E.; Hupp, J. T.; Farha, O. K. Metal-Organic Framework Materials for Light-Harvesting and Energy Transfer. *Chem. Commun.* **2015**, *51* (17), 3501–3510.

(20) Kreno, L. E.; Leong, K.; Farha, O. K.; Allendorf, M.; Van Duyne, R. P.; Hupp, J. T. Metal–Organic Framework Materials as Chemical Sensors. *Chem. Rev.* **2012**, *112* (2), 1105–1125.

(21) Wang, B.; Lv, X.-L.; Feng, D.; Xie, L.-H.; Zhang, J.; Li, M.; Xie, Y.; Li, J.-R.; Zhou, H.-C. Highly Stable Zr(IV)-Based Metal–Organic Frameworks for the Detection and Removal of Antibiotics and Organic Explosives in Water. *J. Am. Chem. Soc.* **2016**, *138* (19), 6204–6216.

(22) Chen, B.; Yang, Z.; Zhu, Y.; Xia, Y. Zeolitic Imidazolate Framework Materials: Recent Progress in Synthesis and Applications. *J. Mater. Chem. A* **2014**, *2* (40), 16811–16831.

(23) Park, K. S.; Ni, Z.; Côté, A. P.; Choi, J. Y.; Huang, R.; Uribe-Romo, F. J.; Chae, H. K.; O'Keeffe, M.; Yaghi, O. M. Exceptional Chemical and Thermal Stability of Zeolitic Imidazolate Frameworks. *Proc. Natl. Acad. Sci.* **2006**, *103* (27), 10186 LP-10191.

(24) Yao, J.; Wang, H. Zeolitic Imidazolate Framework Composite Membranes and Thin Films: Synthesis and Applications. *Chem. Soc. Rev.* **2014**, *43* (13), 4470–4493.

(25) Kwon, H. T.; Jeong, H.-K.; Lee, A. S.; An, H. S.; Lee, J. S. Heteroepitaxially Grown Zeolitic Imidazolate Framework Membranes with Unprecedented Propylene/Propane Separation Performances. *J. Am. Chem. Soc.* **2015**, *137* (38), 12304–12311.

(26) Eum, K.; Jayachandrababu, K. C.; Rashidi, F.; Zhang, K.; Leisen, J.; Graham, S.; Lively, R. P.; Chance, R. R.; Sholl, D. S.; Jones, C. W.; et al. Highly Tunable Molecular Sieving and Adsorption Properties of Mixed-Linker Zeolitic Imidazolate Frameworks. *J. Am. Chem. Soc.* **2015**, *137* (12), 4191–4197.

(27) Li, S.; Huo, F. Metal-Organic Framework Composites: From Fundamentals to Applications. *Nanoscale* **2015**, *7* (17), 7482–7501.

(28) Kitao, T.; Zhang, Y.; Kitagawa, S.; Wang, B.; Uemura, T. Hybridization of MOFs and Polymers. *Chem. Soc. Rev.* **2017**, *46* (11), 3108–3133.

(29) Denny, M. S.; Cohen, S. M. In Situ Modification of Metal–Organic Frameworks in Mixed-Matrix Membranes. *Angew. Chemie Int. Ed.* **2015**, *54* (31), 9029–9032.

(30) Anahid, S.; Beatriz, S.; Damla, K.; Nicole, D.; Tania, R.; Salman, S.; Sara, S.; Le, G. C.; Guillaume, C.; Carlos, T.; et al. Metal Organic Framework Crystals in Mixed-Matrix Membranes: Impact of the Filler Morphology on the Gas Separation Performance. *Adv. Funct. Mater.* **2016**, *26* (18), 3154–3163.

(31) Carne, A.; Carbonell, C.; Imaz, I.; Maspoch, D. Nanoscale Metal-Organic Materials. *Chem. Soc. Rev.* **2011**, *40* (1), 291–305.

(32) Kuo, C.-H.; Tang, Y.; Chou, L.-Y.; Sneed, B. T.; Brodsky, C. N.; Zhao, Z.; Tsung, C.-K. Yolk–Shell Nanocrystal@ZIF-8 Nanostructures for Gas-Phase Heterogeneous Catalysis with Selectivity Control. *J. Am. Chem. Soc.* **2012**, *134* (35), 14345–14348.

(33) Takaaki, T.; Shuhei, F.; Yohei, T.; Kaname, Y.; Seiji, I.; Susumu, K. Nanoporous Nanorods Fabricated by Coordination Modulation and Oriented Attachment Growth. *Angew. Chemie Int. Ed.* **2009**, *48* (26), 4739–4743.

(34) Huang, L.; Zhang, X.; Han, Y.; Wang, Q.; Fang, Y.; Dong, S. In Situ Synthesis of Ultrathin Metal-Organic Framework Nanosheets: A New Method for 2D Metal-Based Nanoporous Carbon Electrocatalysts. *J. Mater. Chem. A* **2017**, *5* (35), 18610–18617.

(35) Xu, L.; Liangcan, H.; Jianzhong, Z.; Jun, G.; Feng, B.; Xiang, M.; Kun, Z.; Yaling, L.; Rui, S.; Zhiyong, T. Solar-Light-Driven Renewable Butanol Separation by Core–Shell Ag@ZIF-8 Nanowires. *Adv. Mater.* **2015**, *27* (21), 3273–3277.

(36) Rodenas, T.; Luz, I.; Prieto, G.; Seoane, B.; Miro, H.; Corma, A.; Kapteijn, F.; Llabrés i Xamena, F. X.; Gascon, J. Metal–Organic Framework Nanosheets in Polymer Composite Materials for Gas Separation. *Nat. Mater.* **2014**, *14*, 48.

(37) Tae-Lim, C.; H., G. R. Controlled Living Ring-Opening-Metathesis Polymerization by a Fast-Initiating Ruthenium Catalyst. *Angew. Chemie Int. Ed.* **2003**, *42* (15), 1743–1746.

(38) Arbulu, R. C.; Jiang, Y.; Peterson, E. J.; Qin, Y. Metal–Organic Framework (MOF) Nanorods, Nanotubes, and Nanowires. *Angew. Chemie Int. Ed.* **2018**, *0* (0).

(39) He, M.; Yao, J.; Li, L.; Zhong, Z.; Chen, F.; Wang, H. Aqueous Solution Synthesis of ZIF-8 Films on a Porous Nylon Substrate by Contra-Diffusion Method. *Microporous Mesoporous Mater.* **2013**, *179*, 10–16.

(40) Yao, J.; Dong, D.; Li, D.; He, L.; Xu, G.; Wang, H. Contra-Diffusion Synthesis of ZIF-8 Films on a Polymer Substrate. *Chem. Commun.* **2011**, *47* (9), 2559–2561.

(41) Shamsaei, E.; Lin, X.; Low, Z.-X.; Abbasi, Z.; Hu, Y.; Liu, J. Z.; Wang, H. Aqueous Phase Synthesis of ZIF-8 Membrane with Controllable Location on an Asymmetrically Porous Polymer Substrate. *ACS Appl. Mater. Interfaces* **2016**, *8* (9), 6236–6244.

(42) Li, Y.; Wee, L. H.; Volodin, A.; Martens, J. A.; Vankelecom, I. F. J. Polymer Supported ZIF-8 Membranes Prepared via an Interfacial Synthesis Method. *Chem. Commun.* **2015**, *51* (5), 918–920.

(43) Martin, C. R. Nanomaterials: A Membrane-Based Synthetic Approach. *Science (80-.).* **1994**, *266* (5193), 1961 LP-1966.

(44) C. Hulteen, J.; Martin, C. R. A General Template-Based Method for the Preparation of Nanomaterials. *J. Mater. Chem.* **1997**, *7* (7), 1075–1087.

(45) R., M. C. Template Synthesis of Polymeric and Metal Microtubules. *Adv. Mater.* **2004**, *3* (9), 457–459.

(46) Bux, H.; Feldhoff, A.; Cravillon, J.; Wiebcke, M.; Li, Y.-S.; Caro, J. Oriented

Zeolitic Imidazolate Framework-8 Membrane with Sharp H2/C3H8 Molecular Sieve Separation. *Chem. Mater.* **2011**, *23* (8), 2262–2269.

(47) Chuantao, H.; Qin, X.; Jinyun, P.; Zhengping, J.; Xiaoya, H. (110)-Oriented ZIF-8 Thin Films on ITO with Controllable Thickness. *ChemPhysChem* **2012**, *14* (1), 140–144.

(48) Wiktor, C.; Meledina, M.; Turner, S.; Lebedev, O. I.; Fischer, R. A. Transmission Electron Microscopy on Metal-Organic Frameworks - a Review. *J. Mater. Chem. A* **2017**, *5* (29), 14969–14989.

(49) Rietveld, H. M. A Profile Refinement Method for Nuclear and Magnetic Structures. *J. Appl. Crystallogr.* **1969**, *2* (2), 65–71.

(50) Williamson, G. K.; Hall, W. H. X-Ray Line Broadening from Filed Aluminium and Wolfram. *Acta Metall.* **1953**, *1* (1), 22–31.

(51) Emil, Z. Determination of the Degree of Preferred Orientation within the March–Dollase Approach. *J. Appl. Crystallogr.* **2009**, *42* (3), 513–518.

(52) Lu, G.; Li, S.; Guo, Z.; Farha, O. K.; Hauser, B. G.; Qi, X.; Wang, Y.; Wang, X.; Han, S.; Liu, X.; et al. Imparting Functionality to a Metal–Organic Framework Material by Controlled Nanoparticle Encapsulation. *Nat. Chem.* **2012**, *4*, 310.

(53) Jiang, Q.; Ward, M. D. Crystallization under Nanoscale Confinement. *Chem. Soc. Rev.* **2014**, *43* (7), 2066–2079.

(54) Cravillon, J.; Schroder, C. A.; Bux, H.; Rothkirch, A.; Caro, J.; Wiebcke, M. Formate Modulated Solvothermal Synthesis of ZIF-8 Investigated Using Time-

Resolved in Situ X-Ray Diffraction and Scanning Electron Microscopy. *CrystEngComm* **2012**, *14* (2), 492–498.

(55) Jin-Oh, K.; Kyoung-Ik, M.; Hyunwoo, N.; Dong-Hwi, K.; Soo-Young, P.; Dong-Pyo, K. Direct Fabrication of Free-Standing MOF Superstructures with Desired Shapes by Micro-Confined Interfacial Synthesis. *Angew. Chemie Int. Ed.* **2016**, *55* (25), 7116–7120.

(56) Peinemann, K.-V.; Abetz, V.; Simon, P. F. W. Asymmetric Superstructure Formed in a Block Copolymer via Phase Separation. *Nat. Mater.* **2007**, *6*, 992.

(57) Zhikun, Z.; Ronny, G.; Xinliang, F. Synthetic Two-Dimensional Materials: A New Paradigm of Membranes for Ultimate Separation. *Adv. Mater.* **2016**, *28* (31), 6529–6545.

(58) Bielawski, C. W.; Grubbs, R. H. Living Ring-Opening Metathesis Polymerization. *Prog. Polym. Sci.* **2007**, *32* (1), 1–29.

(59) Lee, L.-B. W.; Register, R. A. Hydrogenated Ring-Opened Polynorbornene: A Highly Crystalline Atactic Polymer. *Macromolecules* **2005**, *38* (4), 1216–1222.

(60) Sanford, M. S.; Love, J. A.; Grubbs, R. H. Mechanism and Activity of Ruthenium Olefin Metathesis Catalysts. *J. Am. Chem. Soc.* **2001**, *123* (27), 6543–6554.

(61) Rule, J. D.; Moore, J. S. ROMP Reactivity of Endo- and Exo-Dicyclopentadiene. *Macromolecules* **2002**, *35* (21), 7878–7882.

(62) Thirtha, V.; Lehman, R.; Nosker, T. Morphological Effects on Glass Transition Behavior in Selected Immiscible Blends of Amorphous and Semicrystalline

Polymers. *Polymer (Guildf).* **2006**, *47* (15), 5392–5401.